A planar microfluidic mixer based on logarithmic spirals

A planar microfluidic mixer based on logarithmic spirals

Thomas Scherr[1], Christian Quitadamo[2], Preston Tesvich[2], Daniel Sang-Won Park[2], Terrence Tiersch[3], Daniel Hayes[2], Jin-Woo Choi[4], Krishnaswamy Nandakumar[1] and W Todd Monroe[2]

[1] Cain Department of Chemical Engineering, Louisiana State University, 110 South Stadium Drive, Baton Rouge, LA 70803, USA
[2] Department of Biological and Agricultural Engineering, Louisiana State University and LSU AgCenter, 163 EB Doran Bldg, Baton Rouge, LA 70803, USA
[3] Aquaculture Research Station, Louisiana State University Agricultural Center, 2410 Ben Hur Road, Baton Rouge, LA 70820, USA
[4] Department of Electrical and Computer Engineering, Louisiana State University, 102 Electrical Engineering Building, Baton Rouge, LA 70803, USA

E-mail: tmonroe@lsu.edu

Abstract
A passive, planar micromixer design based on logarithmic spirals is presented. The device was fabricated using polydimethylsiloxane soft photolithography techniques, and mixing performance was characterized via numerical simulation and fluorescent microscopy. Mixing efficiency initially declined as the Reynolds number increased, and this trend continued until a Reynolds number of 15 where a minimum was reached at 53%. Mixing efficiency then began to increase reaching a maximum mixing efficiency of 86% at $Re = 67$. Three-dimensional (3D) simulations of fluid mixing in this design were compared to other planar geometries such as the Archimedes spiral and Meandering-S mixers. The implementation of logarithmic curvature offers several unique advantages that enhance mixing, namely a variable cross-sectional area and a logarithmically varying radius of curvature that creates 3D Dean vortices. These flow phenomena were observed in simulations with multilayered fluid folding and validated with confocal microscopy. This design provides improved mixing performance over a broader range of Reynolds numbers than other reported planar mixers, all while avoiding external force fields, more complicated fabrication processes and the introduction of flow obstructions or cavities that may unintentionally affect sensitive or particulate-containing samples. Due to the planar design requiring only single-step lithographic features, this compact geometry could be easily implemented into existing micro-total analysis systems requiring effective rapid mixing.

S Online supplementary data available from stacks.iop.org/JMM/22/055019/mmedia

(Some figures may appear in colour only in the online journal)

1. Introduction

The microfluidic-based manipulation of fluids and particles on a sub-millimeter scale continues to emerge as a unique yet interdisciplinary field. Scientists from a variety of disciplines find microfluidics attractive for a wide range of benefits, including small requisite sample volumes and fast analysis times. At their inception, it was thought that microdevices would serve to miniaturize their macro-scale counterparts and scaled-down micropumps, microvalves and micromixers have been demonstrated [1]. Microfluidics researchers envisioned that these devices could be linked together to miniaturize and automate macro-scale assays on a chip scale, inspiring names such as lab-on-a-chip and micro-total analysis system (μTAS) [1, 2]. Broadly these types of devices are often referred to as biological micro-electro-mechanical systems (Bio-MEMS).

Despite the advances made in recent years, mixing on the micro-scale remains a challenge. In typical microchannel flows, the lack of turbulence, evidenced by very low Reynolds numbers (1), constrains mixing to the natural timescale of diffusion. Peclet numbers, defined as the ratio of convective to diffusive transport, are typically very large in microfluidic applications, where transport is dominated by convection. Consequently, mixing does not readily occur in micro-scale flows. As a result, a dedicated active or passive micromixing element is an integral part of most μTAS and Bio-MEMS devices [3, 4].

$$Re = \frac{\rho U a}{\mu}. \qquad (1)$$

In (1), ρ is the fluid density, U is the fluid velocity, a is the characteristic channel dimension and μ is the fluid viscosity.

Several active micromixers, which involve the use of an external field or force to increase convective motion in fluids [5], have been reported and can be highly effective over short timescales using techniques such as electrokinetic flow, electromagnetic disruption, a thermal bubble micropump and ultrasonic disruption [6–10]. However, these mixers are typically more difficult to fabricate and operate due to costly fabrication techniques and supporting external equipment. As a result, these mixers are typically limited to laboratory implementation and rarely extend to widespread application in μTAS devices.

Passive micromixers do not require external inputs and instead utilize various geometrical features to achieve mixing. In lamination mixers, the channel splits and later recombines the flow [4, 11, 12]; other passive micromixing studies have addressed how fluid folding in diverging channels impacts mixing [3]; some mixers introduce obstacles or cavities in the channel which discretely change the cross-sectional area and create recirculations at higher *Re* that drive mixing [13, 4, 14, 15]. Similar to lamination, hydrodynamic focusing designs utilize sheath streams to confine a concentrated sample stream to a smaller width whereby mixing can occur more rapidly over smaller diffusion distances [16, 17]. Curved microchannels can induce mixing by the generation of secondary flows and interfacial stretching [18, 11, 19, 14] that can be quantified by the Dean number

$$De = Re \sqrt{\frac{a}{R_c}}. \qquad (2)$$

In (2), *Re* is the Reynolds number, *a* is the characteristic channel length and R_c is the radius of curvature.

Recent reviews highlight the need for accurate quantification of micromixer performance and describe several appropriate experimental techniques [20, 21]. Options for reporting mixing performance are more plentiful for computational work, where velocity and species concentration data are available throughout an entire computational domain. More recent computational works have invoked tracer particle tracking with entropic characterization [22, 23]. This method is particularly suited to higher Peclet number flows, as tracer particles follow fluid streamlines and are devoid of any species diffusion. Experimentally, microscopy is the most common technique to analyze mixing. Methods

utilizing standard fluorescent microscopy and dyes measure the summed fluorescent intensity in a vertical column at each pixel in the image, rendering the three-dimensional (3D) data space to a two-dimensional (2D) image. Typically, a transverse linescan is used to generate a plot along a line orthogonal to the flow at the mixer inlets and outlets. This method potentially overestimates mixing performance when the flow profile is distorted in such a way that horizontal striations of non-mixed solute layer on top of one another and appear mixed. To quantitatively evaluate the performance of micromixers, we will use the mixing performance expression given by [24] due to its ease of applicability to both numerical and experimental data

$$\eta = \left[1 - \frac{\int \left| \overline{C}_i^{\text{out}} - C^{\text{mix}} \right| \mathrm{d}y}{\int \left| \overline{C}_i^{\text{in}} - C^{\text{mix}} \right| \mathrm{d}y} \right] \times 100\%. \qquad (3)$$

In (3), C^{mix} is the concentration of a perfectly mixed solution, $\overline{C}_i^{\text{out}}$ and $\overline{C}_i^{\text{in}}$ are the depth-averaged concentrations along the inlet and outlet in the transverse (*y*) direction. This expression is appropriate for experimental images where pixel spacing is uniform, or numerical studies where grid spacing may be non-uniform.

In this study, we present and characterize a passive micromixer named sequential logarithmic mixing apparatus (SeLMA). A prominent element of the mixer design is the use of logarithmic curvature throughout the channel length (figure 1). The utilization of logarithmic curvature has several key advantages: the variable cross-sectional area increases the interfacial stretching and fluid folding, the curvature creates secondary Dean flows and the reversal of the curvature reverses the direction of the secondary flow, thus increasing the convective mixing. We found that logarithmic curvature offers high mixing performance while avoiding external force fields or channel obstructions that could potentially disrupt biological macro-molecules or live cells used in Bio-MEMS applications. Finally, the planar design can be produced by facile single-layer lithography fabrication methods.

2. Design

2.1. Device parameters

The SeLMA micromixer has three 200 μm wide inlets with two sheath streams that are perpendicular to a central sample stream and a constant channel depth of 50 μm throughout. The spiral curves of the channel walls (beginning 800 μm after the junction of the inlets) were inspired from the characteristic polar formula of a logarithmic spiral

$$r = a\mathrm{e}^{b\theta} + C. \qquad (4)$$

There are a variety of curve shapes that can be derived from (4). For instance, setting $a = 0$ will provide a constant radius of curvature at a fixed *C*. Setting $a = \theta$, $b = 0$ and *C* equal to a constant will provide a linearly changing radius of curvature. For non-zero *a*, *b* and *C*, the curve takes the shape of a logarithmic spiral. Since the mixer contains spirals in series, the coefficients used were modified as necessary to ensure continuity of channel width at the junctions of the curves.
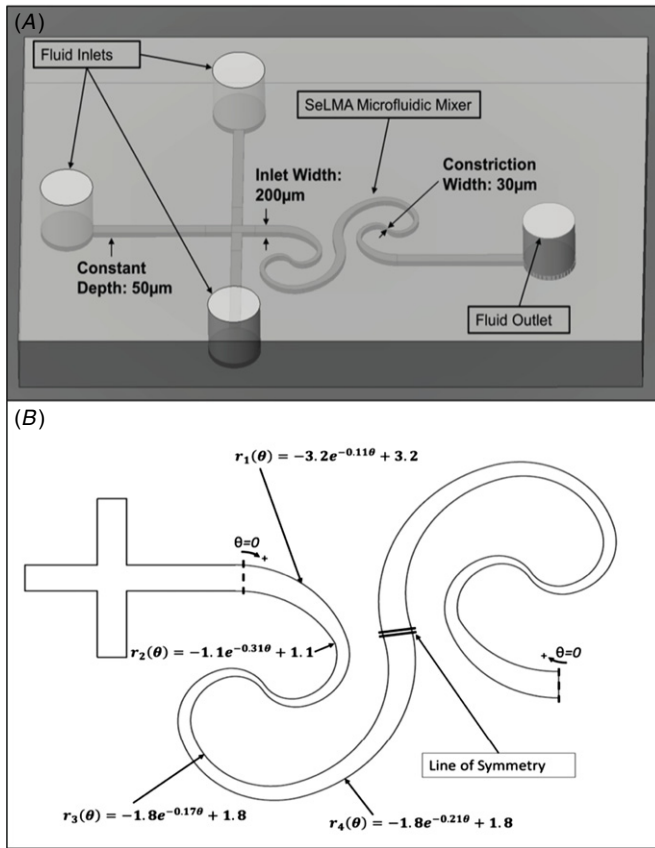
Figure 1. (*A*) Diagram of the SeLMA device schematic showing planar geometry with logarithmic curves to increase mixing by inducing Dean secondary flow vortices. (*B*) 2D schematic of SeLMA showing curve geometry. Fitted polar formulas, such as (4), are given in the units of millimeter.

Two pairs of curves, as seen in figure 1(*B*), are joined at the constriction point. The first pair of curves are developed from $\pi/2 < \theta < 3\pi/2$, and then rotated 180° counterclockwise where the terminal end of the spirals interfaces with the straight channel (800 μm after the junction of the inlets). At the origin of these two curves, another pair of spirals are built from $\pi/2 < \theta < 2\pi$. The curves are copied, mirrored and joined by splines at the point of matching cross-sectional area to create the second half of the SeLMA system. This creates a continuously curved channel, with a dynamic radius of curvature as well as a dynamic cross-sectional area. The projected horizontal area on which the mixing channel is developed is approximately 3 mm × 5 mm with a center channel streamline length of 12 mm.

2.2. Mixing mechanisms

SeLMA incorporates three specific mechanisms to augment mixing performance. While the logarithmic change in the radius of curvature provides a continuously changing cross-sectional area to the mixer, it is also responsible for the formation of Dean vortices (present in all curved channels). Additionally, the three perpendicular inlets provide hydrodynamic focusing. It is hypothesized that: (1) the variable channel width will create fluid stretching; (2) as the Dean

number increases, counter-rotating vortices are expected to increase the mixing performance; (3) the hydrodynamic focusing coupled with the Dean vortices will allow this convective transport to occur in two opposite directions.

A model of the Dean number as a function of position throughout a quarter of SeLMA (after the first constriction point), as well as through a control channel of equivalent maximum radius of curvature and cross-sectional area, illustrates the exploitation of logarithmic curvature (figure 2). After converting polar equations (4) to parametric equations $x(t)$ and $y(t)$, the radius of curvature can be calculated by

$$R_c(t) = \frac{(x'^2 + y'^2)^{3/2}}{|x'y'' - y'x''|}, \tag{5}$$

where all derivatives are calculated with respect to the parameter t. Using this as well as the calculated channel width as a function of position, the two examples were modeled at Reynolds numbers of 5 and 10.

In the control channel of constant radius and constant cross-sectional area, the Dean number remained constant along the length of the channel at a given Reynolds number. Comparatively, the Dean number increased in SeLMA (bottom right in figure 2) reaching its maximum at the constriction point. The log-curved channel did not have a constant cross-sectional area or a constant radius of curvature; both must be evaluated locally using the distance formula and (5). As expected, where the local width decreased, the Reynolds number increased, as well as the Dean number. Furthermore, increasing the Reynolds number in the channel increased the Dean number proportionally. This comparison illustrates the impact of curved geometries and decreasing cross-section on the Dean number which is tenfold greater than the most similar control geometry.

3. Methods

3.1. Numerical simulations

The computational fluid dynamics package Ansys FLUENT was used to solve for the flow field in SeLMA and other micromixers. The structures were drawn in AutoCAD 2010 (Autodesk, Inc., San Rafael, CA), meshed in ICEM v12.1 (Ansys, Inc., Canonsburg, PA) and solved in FLUENT v12.1 (Ansys, Inc., Canonsburg, PA). Using the finite volume method, the steady-state continuity equation, momentum balance and species continuity equation (6)–(8) were solved numerically.

$$\rho \nabla \cdot (\mathbf{v}) = 0 \tag{6}$$

$$\rho (\mathbf{v} \cdot \nabla) \mathbf{v} = -\nabla p + \mu \nabla^2 \mathbf{v} \tag{7}$$

$$\mathbf{v} \cdot \nabla C_A = D_{AB} \nabla^2 C_A. \tag{8}$$

Due to the often negligible effects of inertia in microdevices, the left-hand side of (7) is occasionally neglected, resulting in the Stokes equation [25]. In addition, many microdevices are modeled in two dimensions with acceptable accuracy. However, given that the expected Dean flow is an inherently 3D inertial phenomenon, the full 3D equations were solved.
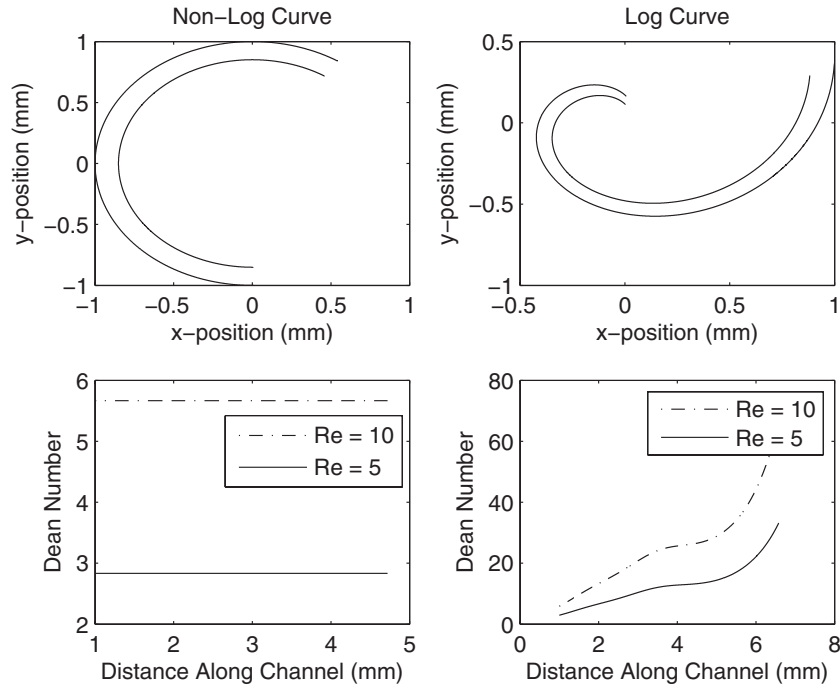
Figure 2. Comparison of Dean numbers within microchannels that are logarithmically curved or of constant curvature, shown as a function of position along the channel.

The entire mixer was simulated, with the inlets truncated after 400 μm—this is beyond sufficient to allow for the flow to become fully developed, while not adding unnecessary computational requirements.

The properties of water at room temperature were used for density and viscosity ($\rho = 10^3$ kg m^{-3}, $\mu = 10^{-3}$ Pa·s), while the diffusion coefficient was set to $D_{AB} = 0.64 \times 10^{-9}$ m^2 s^{-1} corresponding to the diffusivity of fluorescein in water [26]. The normal inlet velocity was varied to evaluate the mixer performance over a range of Reynolds numbers from 1 to 70. The species continuity inlet boundary conditions consisted of a sample stream concentration of 1 mol m^{-3} and sheath concentrations of 0 mol m^{-3}. The specified outlet boundary conditions were a pressure of 0 Pa with no viscous stress and convective flux for the species transport equation. Since the flow was driven by syringe pumps in all the experiments, constant inlet velocity and no-slip boundary conditions at the walls were used. The resulting velocity, pressure and concentration profiles were analyzed using post-processing facilities in FLUENT and MATLAB (MathWorks, Natick, MA). The mesh of each geometry was further refined until they were found to be grid independent; for these 3D simulations, this was achieved with between one and three million nodes depending on the geometry.

3.2. Depth averaging

To make a meaningful comparison of the mixing performance from both simulation data with the experimental data, depth averaging of the simulated concentration field was performed. In experiments, the measured light intensity is proportional to the average concentration in the line of sight of the probe. The depth of focus of a laboratory microscope depends on the magnification and numerical aperture of the objective lens. For a 10× objective lens with a numerical aperture of 0.20, the depth of focus is approximately 35 μm; this is on the order of the depth of a typical microchannel. As previously discussed, pixel intensities are additive over the depth of focus of an imaged area. To mimic this in simulation, the concept of depth averaging was applied, where in a channel of constant depth throughout the mixer, depth-averaged concentrations were computed for comparison with experimental profiles of concentrations in lateral directions.

For 3D simulations, inlets and outlets are represented as 2D planes. The simulations provided discrete data points at computational nodes on these input/output planes. For each position across the width of the outlet, the concentrations are averaged over the depth of the outlet using

$$\overline{C} = \frac{1}{z_2 - z_1} \int_{z_1}^{z_2} C \, \mathrm{d}z, \qquad (9)$$

where z represents the direction of the depth. To span the entire height of the microchannels in SeLMA, z_1 and z_2 were set to 0 and 50 μm, respectively. These depth-averaged concentrations were then used in (3) to calculate the depth-averaged mixing efficiency of the mixer at the outlet.

3.3. Device fabrication

The soft lithography fabrication methods used in this study have been described elsewhere [27]. Briefly AutoCAD was used to design chip geometries, and using a MANN 3600 pattern generator (GSA Corporation, Marietta, GA) a glass–chromium photomask was generated from the imported CAD file. SU-8 master molds were fabricated using a single-step photolithography process. SU-8 2025 (MicroChem Corporation, Newton, MA) was utilized to create a mold

with positive relief structures on a 4 inch silicon wafer (Universitywafer.com, South Boston, MA). Protocols from MicroChem were adapted for the photolithography process [23]. The SU-8 was spin coated on the Si wafer to achieve a thickness of 50 μm. The wafers were then pre-baked and exposed via a Quintel UL7000-OBS system to 365 nm UV light with an intensity of 8.57 mW cm^{-2}, an effective dose of 500 mJ cm^{-2}. Following exposure and post-exposure baking, the wafers were developed with SU-8 developer (MicroChem Corporation, Newton, MA), rinsed with isopropyl alcohol, and dried in air. This entire process was completed within a class 100 clean room at the Center for Advanced Microstructures and Devices, Louisiana State University.

Final devices were then fabricated from polydimethylsiloxane (PDMS), Sylgard 184 (Dow Corning, Midland, MI), at a ratio of 10:1 polymer to curing agent by weight on the previously fabricated SU-8 master. This was allowed to cure for 8 h at 33 °C before coring fluidic access ports using a Harris UniCore^{TM}, tip diameter of 1.0 mm (Harris, Redding, CA). The devices and plain 1 inch × 3 inch, 1 mm thick glass slides (VWR, Radnor, PA) were then plasma oxidized with a Harrick Plasma Cleaner on the high setting (PDC-32G Harrick Plasma, Ithaca, NY) and bonded by applying pressure and baking again at 60 °C for 30 min. Tygon tubing (0.03 inch ID) (Cole-Parmer, Vernon Hills, IL) was used to connect the three inlets of the device to a syringe pump (KD Scientific, Holliston, MA) and 5 mL syringes. The outlet emptied into a waste dish.

3.4. Device validation

Fluorescent microscopy using 46 μM fluorescein sodium salt pumped through the center inlet channel and DI water in the outer channel inlets was used to evaluate mixing. Images were collected using 10× magnification (Nikon Eclipse TS100 Microscope), with a fluorescent lamp excitation of 492 and 520 nm emission, and an exposure time of 500 ms (Lambda BG-4). Image processing and analysis were conducted using Metamorph Imaging software v7.5.6 (Molecular Devices, Inc., Sunnyvale, CA) and 16-bit resolution. A cross-sectional pixel intensity plot was created for the outlet and all three inlets; the data for the inlets were combined into one inlet vector, and mixing efficiencies were calculated using (3). Mixing performance was evaluated at the outlet in increments of $Re = 1$. A maximum Reynolds number of 70 was selected based on the potential applications of SeLMA in microdevices, and previously used Re values from similar mixers [28].

3.5. Confocal imaging

Confocal imaging was used to create a 3D image volume of the cross-sectional area of the channel and secondary flow effects throughout the micromixer. A scanning laser confocal microscope (Leica TCS SP2) with a 10× objective was used to capture Z-stacks at various points along the mixer channel (inlet, curve leading to constriction, constriction and outlet of the mixer,) at selected Reynolds numbers. A total stack height of 30 μm was imaged with 0.5 μm slice thickness. Image J (NIH, Bethesda, MD) software was used to combine the

stacks and transect at the desired cross-sectional area of the micromixer, orthogonal to the direction of flow.

4. Results and discussion

4.1. Simulation

From inspection of (2), it is clear that the Dean number increases as the Reynolds number increases or as the radius of curvature decreases. The logarithmic curvature in SeLMA also provided the mixer with a continuously changing radius of curvature, as well as continuously variable cross-sectional area. As the fluid approached the first constriction point of the mixer, the cross-sectional area and the radius of curvature decreased. As the cross-section decreased, the Reynolds number increased, which proportionally increased the Dean number. The radius of decreasing curvature increased the Dean number proportional to the 1/2 power of the radius of curvature. It was thus expected that the magnitude of Dean vortices would be greatest near the constriction points.

To investigate the presence of Dean flows in SeLMA, plots of the z-velocity were analyzed (figure 3), where positive z is toward the top of the microchannel. On the top (figure 3(*A*)), the classic Dean vortices are visible in the x–z plane: following the direction of the flow, there is positive z-velocity in the top right and bottom left of the plane and negative z-velocity in the top left and bottom right of the plane. This illustrates two vortices separated by a plane of symmetry at the vertical midplane of the mixer (figure 3(*A*) inset). On the bottom (figure 3(*B*)) is a plot of z-velocity at a constant height of 40 μm from the bottom of the mixer on a constant z-plane (chosen to avoid the plane of symmetry near the midplane). Following the fluid flow in this plane, prior to the constriction point the fluid on the right half of the channel had a negative z-velocity, while the fluid on the left half of the channel had a positive z-velocity. At the constriction point, the radius of curvature of the mixer changes directions. After the constriction point, these z-velocities were reversed in direction.

Other curved channel mixers have been reported that take advantage of the flow phenomena predicted in SeLMA, such as the Archimedes spiral [19] and the Meandering-S mixer [18]. Difficulty arises in comparing micromixer designs due to differences in channel dimensions, Reynolds numbers and the expressions used to evaluate mixing performance. To make the closest comparisons, these mixers were adapted from the literature and scaled for appropriate comparison to SeLMA. All designs were evaluated with three inlets, 200 μm wide channels and a pathlength of approximately 12 mm and a channel depth of 50 μm (simulation geometries shown in the supplementary material, available from stacks.iop.org/jmm/22/055019/mmedia).

The secondary flows present in all curved mixers improved mixing performance after a certain Re threshold (figure 4(*A*)). At this transition point, the mixing could be attributed to convection rather than diffusion-based mass transport. A straight T-channel is shown for comparison; without any mechanism to enhance mixing, the mixing performance monotonically decreases as Re increases. The
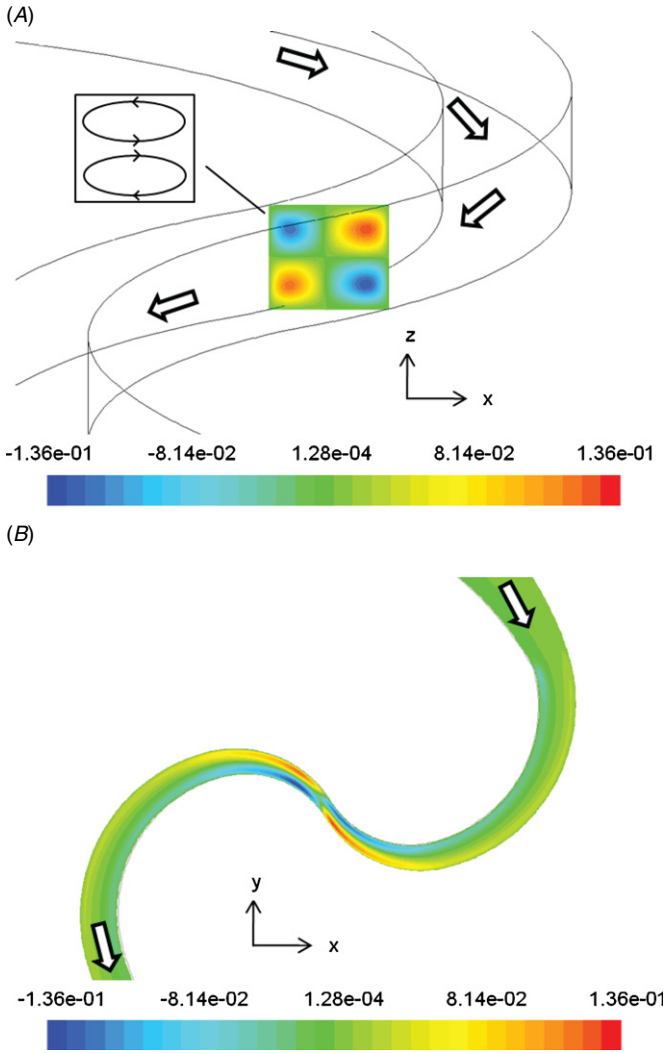
(A)

(B)

Figure 3. Simulation images of *z*-velocity at the first constriction of the mixer (units are m/s). (A) The direction of flow is from top to bottom. Inset shows that this *z*-velocity profile is consistent with typical Dean vortices. (B) The plane is taken at a constant height of 40 μm from the bottom of the channel.

logarithmic curvature in SeLMA outperformed the other mixers over the entire range of *Re* tested.

Pressure drops of the simulated mixers are calculated by integrating the pressure in nodes at the inlets, summing the three inlets to find a total inlet pressure and subtracting the integrated pressure of nodes at the outlet. These are shown for the tested range of Reynolds numbers in figure 4(*B*). As expected, the pressure drop across SeLMA is consistently higher than that of the other mixers used for comparison. This is a direct result of the constrictions in SeLMA. However, figure 4(*B*) shows that SeLMA's pressure drop is only slightly higher in magnitude than that of the other curved mixers at lower Reynolds numbers. The disparity between pressure drops across SeLMA, the Meandering-S and Archimedes Spiral increases sharply after a Reynolds number of 25. While the higher pressure drop required is a drawback, we were able to operate our device up to Reynolds numbers of 70 with no observed leakage at the fluid inlet and outlet connections. These connections were not sealed in any way
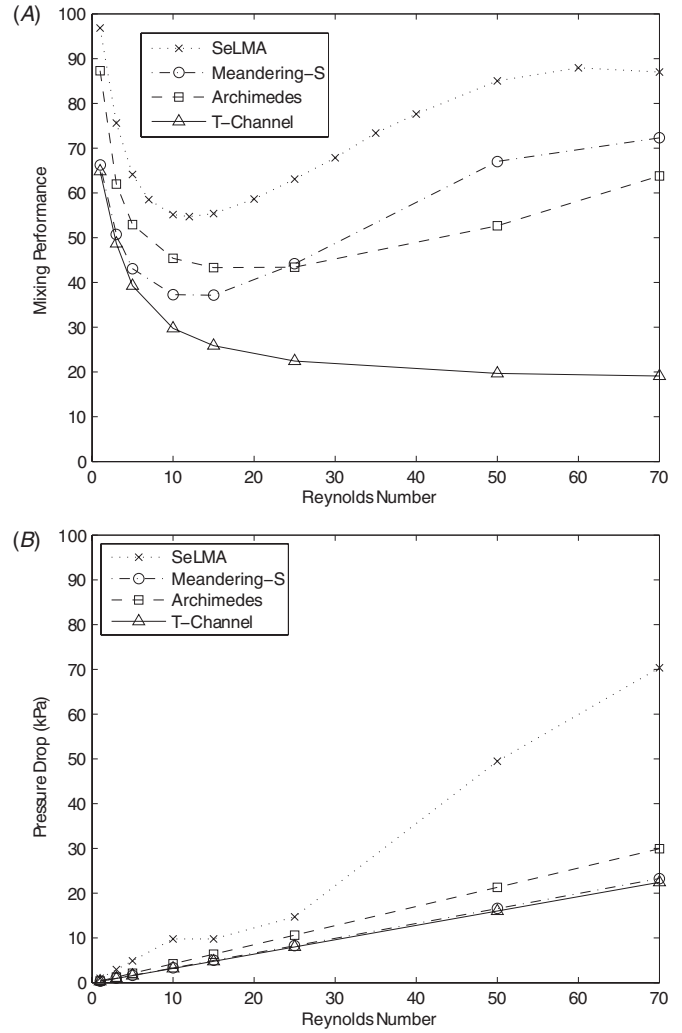
(A)

(B)

Figure 4. (A) Simulation results of mixing performance in SeLMA and other curved channel micromixers. Mixer designs from previous reports were adapted to have the same number of inlets, similar dimensions and path lengths as SeLMA. (B) Simulated pressure drops for the same mixers.

Table 1. Comparison of mixing performance and mixing efficiency per mm mixing path length, at *Re* = 70, evaluated numerically in SeLMA and a selection of micromixers adapted from the literature: the Archimedes spiral [19], the Meandering-S [18] and a T-channel.

Micromixer	η (%)	$\frac{\eta}{L}$ (%/mm)
SeLMA	87.015	6.8911
Meandering-S	72.31	6.02
Archimedes	63.80	5.32
T-channel	19.11	1.59

beyond tight fitting Tygon into PDMS. For the benchscale applications envisioned for this micromixer, the pressure drop seems manageable given the increase in mixing performance it provides.

The comparison of SeLMA versus mixers adapted from the literature was also made on a per unit length basis, shown in table 1. Commonly, micromixers are reported as having complete mixing after a given number of mixing elements in series. To compare these mixers effectively, the ratio of the reported mixing performance to the mixing path length
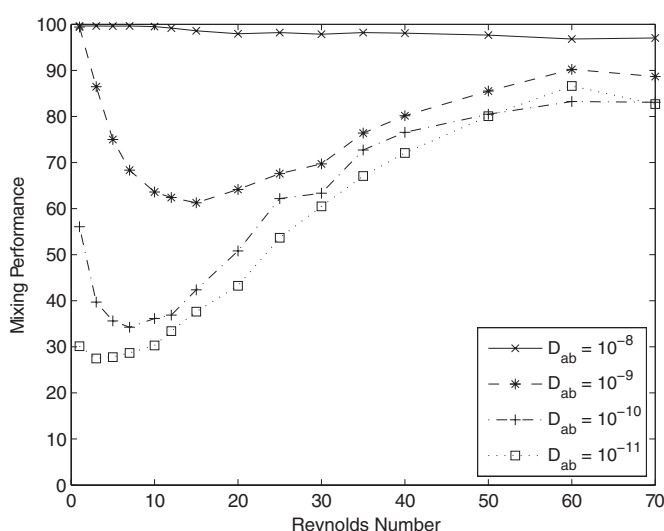
Figure 5. Simulation results over a range of diffusivities.

Figure 6. Comparison of the simulation results to experimental results at the first constriction of SeLMA with a Reynolds number of 40. (*A*) Concentration contour plot taken at the midplane of the device. (*B*) Fluorescent micrograph of fluorescein mixing in SeLMA device. From inspection of the two images, similar flow characteristics can be seen between the simulated and experimental images. Most notable is the fluid diversion to the channel walls as the channel width decreases.

was used to standardize mixing performance per unit length (i.e. percentage per mm). We have chosen to highlight the performance at the highest *Re* from each of the simulated mixers. From the comparison, the SeLMA mixer had a higher mixing performance per unit length and thus requires a shorter path length to mix the same fluid effectively.

Samples introduced to micromixers can have widely varying diffusion coefficients which could affect mixing performance. This parameter's impact on mixing in SeLMA was numerically investigated over four orders of magnitude of diffusivity (figure 5). For very high diffusivities mixing performance is exceptional over the entire range of *Re*, not dropping below 96%. As diffusivity decreases, the expected behavior is seen; the mixing performance initially decreases, reaches a minimum and then begins to increase again as the Reynolds number increases. Particularly encouraging is that all four diffusivities tested reach above 80% at the highest Reynolds numbers tested. Figure 5 does show an artifact that was discussed earlier: distortion of the fluid profile can result in unmixed layers of fluid that when depth averaged would be perceived as mixed. This is seen at an *Re* of 60 where solute of D_{ab} of 10^{-11} m^2 s^{-1} appears to have higher mixing performance than that of 10^{-10} m^2 s^{-1}. A species with a diffusivity of an order of magnitude lower diffusivity should not result in a higher mixing performance. The fact that this artifact was only observed in this instance suggests the depth averaging is acceptable in this analysis. The results from figure 5 display SeLMA's versatility with respect to the types of samples that could be mixed.

4.2. Experimental details

The SeLMA simulations were validated by device fabrication and observation via fluorescent microscopy (figure 6). Fluorescein, introduced in the center of the hydrodynamically focused streams, was initially contained in the middle of the channel, with limited dispersion (figure 6(*A*)). As the channel curvature increases, the fluorescein began to distribute,
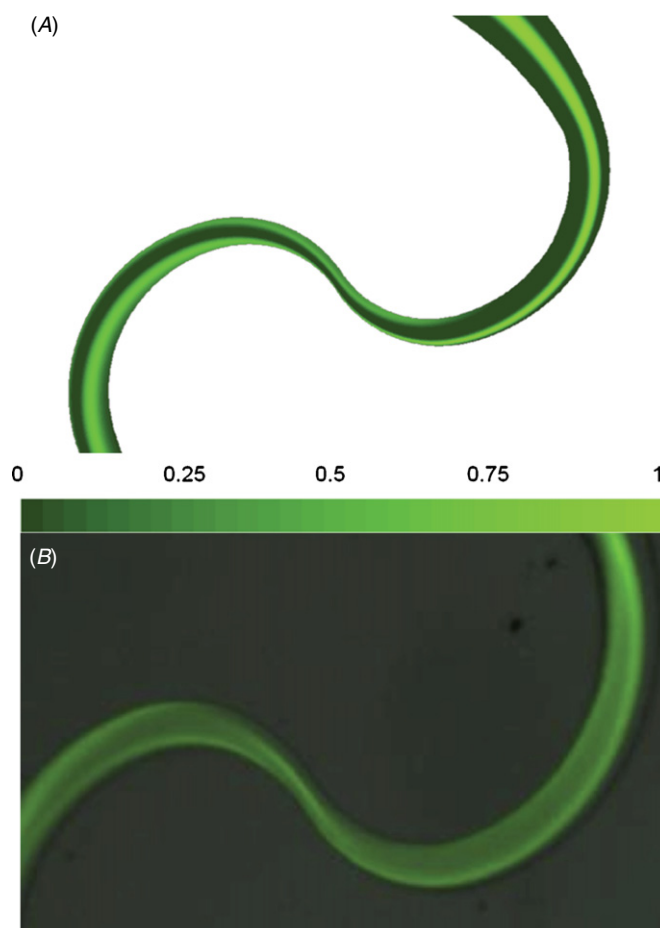
spreading out toward the outside wall of the channel. Near the constriction, a band of higher intensity was observed, presumably due to a rotation of the broadened band due to the Dean flow, which then disperses again after the constriction point. Visualization of a concentration contour plot in simulations revealed a similar pattern to that observed experimentally, showing that prior to the increasing curvature and constriction, the fluorescein was constrained to the middle of the channel, whereas afterward, the flow transitioned to the side walls and dispersed in a helical pattern (figure 6(*B*)).

As noted across mixers that utilize the Dean flow, there is a transition between diffusive mixing at low *Re* to convective components at higher *Re*. This behavior was compared between simulation and experimental testing in SeLMA (figure 7). There was a strong correlation between experimental and simulated mixing performance, which initially decreased as *Re* increased, with a minima occurring at a Reynolds number of approximately 15. Indicative of a regime change, the mixing efficiency began to increase as the
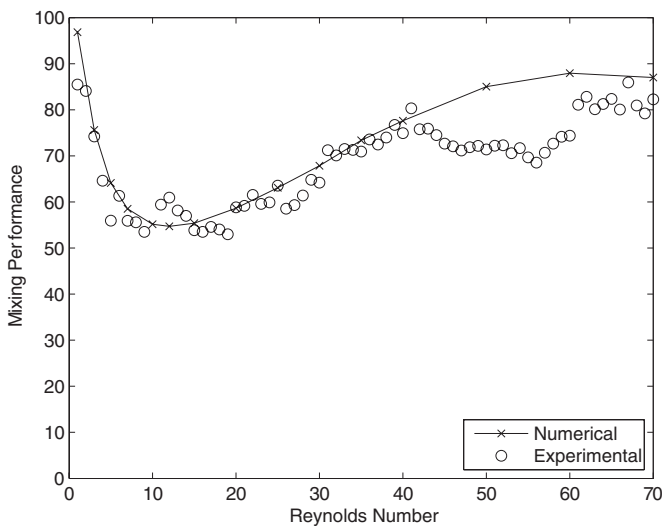
Figure 7. Comparison between simulation and fluorescent microscopy results of mixing performance in SeLMA.

Reynolds number increased beyond this threshold. Above an *Re* of 15, it is thought that the secondary flows in the mixer become dominant and drive the mixing in the device. In both the simulated and physical experimental devices, the transition from one regime to the other occurs at approximately the same Reynolds number. Deviation between simulation results and those acquired experimentally, particularly at higher *Re*, could be an artifact of the higher velocities on intensity during the relatively long acquisition times employed, or the aforementioned differences between the computational and standard fluorescent microscopy depth averaging of intensity.

4.3. Confocal imaging

Confocal imaging of the SeLMA micromixer provided cross-sectional images of the flow profile during mixing with fluorescein and water (figure 8). Initially at the inlet intersections (figure 8(*A*)), the cross-section showed confinement of fluorescein to the middle stream. As the

curvature increased (figure 8(*B*)), the fluorescein began to stratify transverse to the flow, with significant multilayer folding observed at the constriction point (figure 8(*C*)). At the outlet of SeLMA (figure 8(*D*)), the fluorescein was much more dispersed. Confocal cross-sections were compared at the first constriction of the micromixer at various *Re* (figure 9). As *Re* increased, the development of the complex secondary flows increases. From the confocal imaging results, it can be concluded that as *Re* increases, the degree of secondary flow in the mixer also increases. However, even at low *Re*, bending of the solute band in the direction of the outer curve could be observed to fold the flow streams horizontally (figure 9(*A*)). As Reynolds number increased, this folding becomes more pronounced, with multilayered folding observed at a Reynolds number of 40 (figure 9(*D*)). Confocal imaging of the device provided proof of horizontal fluid flow folding and dispersion and true mixing. Because non-confocal fluorescent microscopy averages depth over the height of the microchannel, as noted before, non-mixed horizontal layers of solute could be perceived as being mixed. Here the cross-sectional dispersion pattern of solute at the mixer outlet, shown experimentally through confocal images (figure 8(*D*)), provides evidence for mixing.

5. Conclusions

Microdevices lacking a mixer rely solely on molecular diffusion, and as such mixing requires channels that can be impractically long. Mixing performance in such devices monotonically decreases as Reynolds number increases, limiting high-throughput processes that require well-mixed solutions. Herein we present a planar passive mixer based on logarithmic spiral geometry. The logarithmic curves can be sequentially arranged to additively increase mixing; thus, the design is termed a sequential logarithmic mixing apparatus (SeLMA). Being planar allows 'one-step' fabrication using traditional photolithography techniques. The logarithmic spirals provided a continuously changing cross-sectional area as well as a continuously changing radius of curvature. The
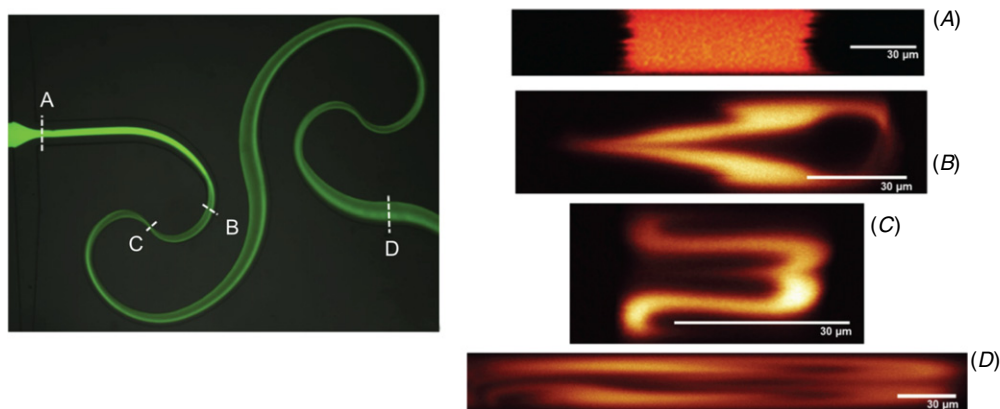

Figure 8. Confocal micrographs of the cross-section of the microchannel at various locations (*A*)–(*D*) throughout the mixer. *Re* = 40. Z-stacks were reconstructed to observe cross-sectional secondary flows at the various locations. (*A*) The cross-section before the mixing structure where no secondary flows are present. As the fluid progressed from (*B*) to (*D*), secondary Dean flows developed. Reconstruction of the cross-section from the z-stack was dependent on the depth and width of the channels being imaged. Because SeLMA has a varying width throughout the mixer, images (*A*)–(*D*) each have different aspect ratios depending on the width of the channel at the imaged location.
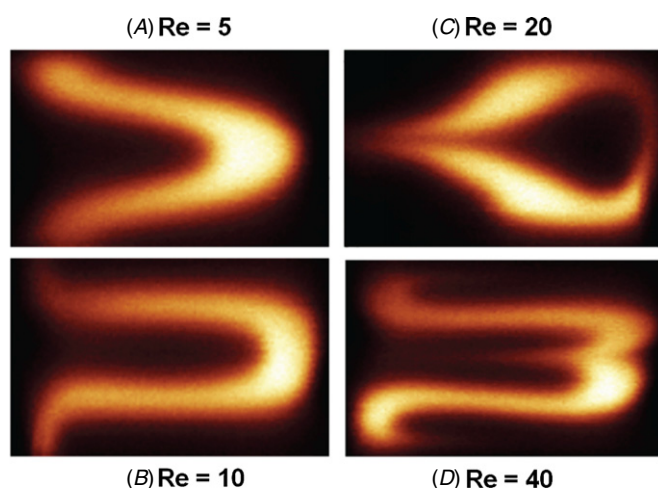
Figure 9. Confocal micrographs of the cross-section at the first constriction point in SeLMA at various Reynolds numbers. Counterclockwise from top left: *Re* = 5, 10, 20 and 40.

combination of these caused advection that dispersed the sheath and sample fluid among one another. This dispersion was larger at higher Reynolds numbers, which yielded higher mixing performance. A transition is clearly seen at a Reynolds number of 15 where the diffusion-based trend gives way to increased mixing at higher *Re*, and a more inertial regime. Initially mixing efficiency decreased to the previously stated minima of 53%, but began to steadily increase to a maximum of 86% at *Re* = 67.

Based on the presented results, the SeLMA micromixer has been shown to be an improvement over existing passive planar micromixer designs. The mixing performance of SeLMA was compared to scaled models of the Archimedes, Meandering-S and a simple T-channel. As noted, the three alternative mixers were scaled appropriately for comparisons. A minimum was observed in all the mixers as Reynolds number increased from 1 to 12, and performance begins to increase for all curved channel mixers past the minima. In comparison, SeLMA displayed improved performance throughout the entire sweep of Reynolds numbers simulated. In particular, SeLMA showed a 10–15% higher efficiency than both the Archimedes and Meandering-S mixer designs at all Reynolds numbers greater than 15. Direct comparison of the mixing performance of SeLMA to previously reported mixing performance is problematic due to differences in experimental designs and protocols. In terms of mixing per unit length, SeLMA proved to most efficiently utilize its pathlength for mixing. SeLMA has a larger pressure drop than comparable mixers, but this pressure drop is manageable given the increase in mixing performance it provides. The geometric features responsible for mixing in SeLMA do not require flow obstructions or cavities as do herringbone-type designs which may affect fragile or particulate-containing samples [29].

Overall, the Dean vortices in SeLMA were shown to exist in simulation, and qualitatively demonstrated via confocal fluorescent microscopy. These secondary flows along with the viscous folding and interfacial stretching, caused by the variable cross-sectional area, drive the mixing performance at higher *Re*. This high level of mixing was observed in numerical experiments over four orders of magnitude of species diffusivity. In future work, we plan to investigate the contributions of the individual coefficients in (4) and their relation to the mixing mechanisms (hydrodynamic focusing, variable cross-sectional area and curvature), and evaluate how this impacts the overall performance of SeLMA. This deconstruction will provide insight into a mechanisms' utility at a particular Reynolds number for future micromixer design. SeLMA lacks obstructions, cavities, or sharp corners that could potentially hold up or damage sensitive biological samples. With the performance stated, and without the need for external drivers and equipment, the SeLMA mixer presented could be implemented into existing μTAS to achieve rapid mixing in a small chip footprint.

Acknowledgments

References

[1] Ho C-M and Tai Y-C 1998 Micro-electro-mechanical systems (MEMS) and fluid flows *Annu. Rev. Fluid Mech.* **30** 579–612

[2] Stone H A, Stroock A D and Ajdari A 2004 Engineering flows in small devices *Annu. Rev. Fluid Mech.* **36** 381–411

[3] Chung C, Choi D, Kim Ju M, Ahn K H and Lee S J 2009 Numerical and experimental studies on the viscous folding in diverging microchannels *Microfluid. Nanofluid.* **8** 767–76

[4] Nguyen N-T and Wu Z 2005 Micromixers: a review *J. Micromech. Microeng.* **15** R1–16

[5] Hessel V, Lowe H and Schonfeld F 2005 Micromixers: a review on passive and active mixing principles *Chem. Eng. Sci.* **60** 2479–501

[6] Tsai J-H and Lin L 2002 Active microfluidic mixer and gas bubble filter driven by thermal bubble micropump *Sensors Actuators A: Phys.* **97–98** 665–71

[7] Wen C-Y, Yeh C-P, Tsai C-H and Fu L-M 2009 Rapid magnetic microfluidic mixer utilizing ac electromagnetic field *Electrophoresis* **30** 4179–86

[8] Wu H-Y and Liu C-H 2005 A novel electrokinetic micromixer *Sensors Actuators A: Phys.* **118** 107–15

[9] Yang Z, Goto H, Matsumoto M and Maeda R 2000 Active micromixer for microfluidic systems using lead-zirconate-titanate(pzt)-generated ultrasonic vibration *Electrophoresis* **21** 116–9

[10] Yang Z, Matsumoto S, Goto H, Matsumoto M and Maeda R 2001 Ultrasonic micromixer for microfluidic systems *Sensors Actuators A: Phys.* **93** 266–72

[11] Sudarsan A P 2006 Multivortex micromixing *Proc. Natl Acad. Sci. USA* **103** 7228–33

[12] Tofteberg T, Skolimowski M, Andreassen E and Geschke O 2010 A novel passive micromixer: lamination in a planar channel system *Microfluid. Nanofluid.* **8** 209–15

[13] Hong C-C, Choi J-W and Ahn C H 2004 A novel in-plane passive microfluidic mixer with modified tesla structures *Lab Chip* **4** 109

[14] Tsai R-T and Wu C-Y 2011 An efficient micromixer based on multidirectional vortices due to baffles and channel curvature *Biomicrofluidics* **5** 014103

[15] Stroock A D 2002 Chaotic mixer for microchannels *Science* **295** 647–51

[16] Gambin Y, Simonnet C, VanDelinder V, Deniz A and Groisman A 2010 Ultrafast microfluidic mixer with three-dimensional flow focusing for studies of biochemical kinetics *Lab Chip* **10** 598

[17] Wang F, Wang H, Wang J, Wang H-Y, Rummel P L, Garimella S V and Lu C 2008 Microfluidic delivery of small molecules into mammalian cells based on hydrodynamic focusing *Biotechnol. Bioeng.* **100** 150–8

[18] Jiang F, Drese K S, Hardt S, Kupper M and Schonfeld F 2004 Helical flows and chaotic mixing in curved micro channels *AIChE J.* **50** 2297–305

[19] Sudarsan A P and Ugaz V M 2006 Fluid mixing in planar spiral microchannels *Lab Chip* **6** 74

[20] Aubin J, Ferrando M and Jiricny V 2010 Current methods for characterising mixing and flow in microchannels *Chem. Eng. Sci.* **65** 2065–93

[21] Johnson T J, Ross D and Locascio L E 2002 Rapid microfluidic mixing *Anal. Chem.* **74** 45–51

[22] Camesasca M, Manas-Zloczower I and Kaufman M 2005 Entropic characterization of mixing in microchannels *J. Micromech. Microeng.* **15** 2038–44

[23] Kang T G and Kwon T H 2004 Colored particle tracking method for mixing analysis of chaotic micromixers *J. Micromech. Microeng.* **14** 891–9

[24] Chang C C and Yang R J 2004 Computational analysis of electrokinetically driven flow mixing in microchannels with patterned blocks *J. Micromech. Microeng.* **14** 550–8

[25] Squires T M and Quake S R 2005 Microfluidics: fluid physics at the nanoliter scale *Rev. Mod. Phys.* **77** 977–1026

[26] Galambos P and Forster F K 1998 Micro-fluidic diffusion coefficient measurement *Proc. Micro Total Analysis Systems* pp 189–91

[27] del Campo A and Greiner C 2007 Su-8: a photoresist for high-aspect-ratio and 3d submicron lithography *J. Micromech. Microeng.* **17** R81–95

[28] Pratt E D, Huang C, Hawkins B G, Gleghorn J P and Kirby B J 2011 Rare cell capture in microfluidic devices *Chem. Eng. Sci.* **66** 1508–22

[29] Park D, Quitadamo C, Tiersch T R and Monroe W T 2011 Microfluidic mixers for standardization of computer-assisted sperm analysis *Cryopreservation in Aquatic Species* 2nd edn (Baton Rouge, LA: World Aquaculture Society)